

Compact Dual-Band SISL Filtering Antennas With High Selectivity Based on Dual Gap-Coupled Patches

Zhirui Zheng¹, Student Member, IEEE, Xiaoheng Tan¹, Daotong Li², Senior Member, IEEE, Mei Li³, Member, IEEE, and Qiang Chen⁴, Senior Member, IEEE

Abstract—In this article, two compact dual-band substrate integrated suspended line (SISL) filtering antennas with high selectivity based on dual gap-coupled patches are proposed. By using a quasi-I-shaped feedline, etching longitudinal slots on two patches placed symmetrically, and connecting a metal strip with both patches through metallized vias, three radiation nulls (RNs) are generated in the stopband. Thus, an excellent dual-band SISL filtering antenna with broadside radiation is achieved, resulting in high selectivity and deep stopband rejection. To further integrate filtering response and dual band with different radiations, a dual-band SISL filtering antenna with broadside and bidirectional beams is realized. Two RNs are introduced near the upper passband with bidirectional beams by folded C-shaped slots and parasitic strips, and the bidirectional beam is formed by inverted currents on both patches. Moreover, by connecting a T-shaped metal strip with both patches through metallized vias, an extra RN is acquired near the lower passband with broadside beams. Therefore, both sharp roll-off and different radiation in the dual band are achieved. The operating mechanism of both designs is analyzed. Two prototypes are fabricated and tested, and good agreement between simulated and tested values is observed.

Index Terms—Compact, dual band, filtering antenna, pattern diversity, substrate integrated suspended line (SISL).

I. INTRODUCTION

AS A new type of transmission line, substrate integrated suspended line (SISL) owns the properties of low loss, low cost, easy integration, easy processing, lightweight, planarization, and self-packaged [1], fully meeting the requirements of modern communication systems. Thus, SISL has

Manuscript received 26 April 2023; revised 6 July 2023; accepted 29 July 2023. Date of publication 8 August 2023; date of current version 6 October 2023. This work was supported in part by the National Natural Science Foundation of China under Grant 61801059, Grant U20A20157, and Grant U20A200726, in part by the FY2021 Japan Society for the Promotion of Science (JSPS) Postdoctoral Fellowship for Research in Japan under Grant P21053, in part by the Grant-in-Aid for JSPS Research Fellow under Grant 21F21053, and in part by the Basic Research and Frontier Exploration Special of Chongqing Natural Science Foundation under Grant cstc2019jcyj-msxmX0350. (Corresponding author: Xiaoheng Tan.)

Zhirui Zheng, Xiaoheng Tan, and Mei Li are with the School of Microelectronics and Communication Engineering, Chongqing University, Chongqing 400044, China (e-mail: zhengzhirui666@163.com; txh@cqu.edu.cn; li.mei@cqu.edu.cn).

Daotong Li is with the School of Microelectronics and Communication Engineering, Chongqing University, Chongqing 400044, China, and also with the Department of Communications Engineering, Tohoku University, Sendai 980-8579, Japan (e-mail: dli@cqu.edu.cn).

Qiang Chen is with the Department of Communications Engineering, Tohoku University, Sendai 980-8579, Japan (e-mail: qiang.chen.a5@tohoku.ac.jp).

Color versions of one or more figures in this article are available at <https://doi.org/10.1109/TAP.2023.3301628>.

Digital Object Identifier 10.1109/TAP.2023.3301628

been widely used to design various of passive and active devices, such as antennas, filters, power dividers, and power amplifiers [2], [3], [4], [5], [6], [7], [8], [9], [10], [11], [12]. In the past decade, many kinds of antennas based on SISL have been reported successively, such as quasi-Yagi antenna [2], dielectric resonator antenna [3], cavity-backed antenna [4], dipole antenna [5], leaky-wave antenna [6], and patch antenna [7], [8], [9]. However, to suppress out-of-band interference, filters need to be cascaded directly with these designs, which inevitably increases the circuit size and insertion loss of the system.

On the one hand, filtering antennas not only decrease the overall size and insertion loss of the system but also improve the antenna bandwidth and the stability of in-band gain [13], [14]. The popular design methods of filtering antennas can be divided into two categories: 1) bandpass filter synthesis, where the antenna acts as a radiator as well as a stage of the resonators and 2) fusion design, where filtering performance is obtained by loading short pins, etching slots, and using parasitic/stacked elements. Based on the aforementioned methods, several SISL filtering antennas have been successfully implemented [15], [16], [17], [18]. In [15], a differentially fed SISL MIMO filtering antenna was presented. By loading parasitic L-shaped resonators near the main radiator and placing a specially designed stacked patches, good filtering performance with three radiation nulls (RNs) was achieved. In [16], by placing a rectangular loop underneath stacked patches, a high-gain filtering SISL antenna with two RNs was obtained. In [17], an SISL filtering antenna with four RNs and enhanced frequency selectivity was attained by using slots, parasitic units, stubs, and stacked patches. To realize a low-cost, miniaturized, and high selective design, a filtering dielectric resonator antenna (FDRA) was first proposed based on SISL [18]. However, these designs only focus on a single operating band. To the best of our knowledge, only one dual-band SISL filtering antenna has been reported to date [19]. Despite three RNs were yielded using stacked/parasitic units, the selectivity of the upper passbands is still poor, especially for the right sideband with positive realized gain. To improve the filtering performance and further reduce the system volume and cost [20], [21], [22], [23], dual-band SISL filtering antennas with high selectivity are highly demanded.

On the other hand, the same or different radiation characteristics can be observed in the dual band of the antenna.

In some cases, antennas with different radiation properties over two bands are required to support different wireless services [24], [25], [26], [27], [28], which avoids the use of different antennas and enables miniaturization of the system. In [24], a dual-band antenna with broadside and bidirectional radiation using a monopole array and four patches was proposed for vehicle communications. In [25], by etching two U-shaped slots and loading a short pin, a single-fed dual-band patch antenna with broadside and bidirectional beams was presented for wireless local area networks (WLANs) applications (indoor and outdoor). Through the use of different radiators, the omnidirectional and unidirectional radiation patterns were achieved in [26], [27], and [28]. However, these dual-band radiation-differentiated antennas have no filtering performance. To the best of our knowledge, filtering performance and dual-band response with different radiations have not been integrated together in the published literature. To avoid the use of additional filters and take into account the good properties of SISL [1], it is very meaningful to design the dual-band radiation-differentiated filtering antenna based on the SISL platform.

In this article, compact dual-band SISL filtering antennas with high selectivity based on dual gap-coupled patches are proposed. Two antennas are included as follows.

1) A dual-band SISL filtering antenna with broadside beams is presented. Two identical rectangular patches are symmetrically placed at both sides of the quasi-I-shaped feedline; thus, an RN is introduced. By etching a longitudinal slot on each patch and connecting two ends of the metal strip with both patches through metallized vias, two extra RNs are generated in the stopband, respectively. As a result, the excellent dual-band filtering performance with three RNs is obtained on the SISL platform, achieving sharp roll-off rates of 577/307/143/436 dB/GHz, deep out-of-band suppression of over 13.7 dB, and high gain of 8.06/9.32 dBi.

2) To further integrate filtering response and dual band with different radiations, a dual-band SISL filtering antenna with broadside and bidirectional beams is proposed. Due to inverted currents on both patches, the bidirectional beam in the upper passband is formed. Two RNs situated at both sides of the upper passband are yielded by using folded C-shaped slots and parasitic strips. Furthermore, after a T-shaped metal strip is connected to both patches through metallized vias, an RN is produced near the lower passband with broadside beams. Thus, the dual-band filtering response with broadside and bidirectional beams is achieved on the SISL platform, resulting in three RNs, high selectivity, high gain of 7.88/7.98 dBi, and different radiations in the dual band. Both prototypes are validated through fabrication and measurement.

II. DUAL-BAND SISL FILTERING ANTENNA WITH BROADSIDE BEAMS

A. Antenna Configuration

The proposed dual-band SISL filtering antenna with broadside radiation is shown in Fig. 1 and named as Proposed Antenna I. In Fig. 1(a), from the 3-D view, five dielectric layers from substrates 1–5 and ten metal layers from G1–G10

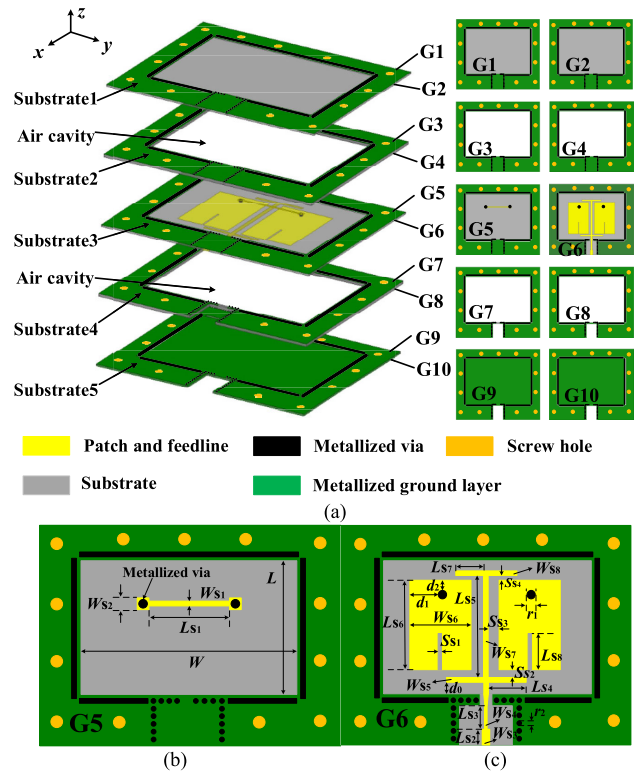


Fig. 1. Configuration of dual-band SISL filtering antenna with broadside radiation (Proposed Antenna I). (a) Three-dimensional view and the configuration of each layer. (b) G5 layer. (c) G6 layer ($L = 35$, $W = 40$, $L_{S1} = 17.55$, $L_{S2} = 4$, $L_{S3} = 6.9$, $L_{S4} = 8.03$, $L_{S5} = 25.81$, $L_{S6} = 23.94$, $L_{S7} = 6.71$, $L_{S8} = 8.84$, $W_{S1} = 0.58$, $W_{S2} = 1.4$, $W_{S3} = 2$, $W_{S4} = 1$, $W_{S5} = 1$, $W_{S6} = 15.6$, $W_{S7} = 1.21$, $W_{S8} = 1.01$, $d_0 = 2.5$, $d_1 = 7.74$, $d_2 = 2.69$, $S_{S1} = 0.46$, $S_{S2} = 0.82$, $S_{S3} = 1.51$, $S_{S4} = 1.05$, $r_1 = 1$, and $r_2 = 0.6$. Unit: mm).

are contained. Substrates 1, 3, and 5 all adopt the material of Rogers 4350 with the relative dielectric constant of 3.48, loss tangent of 0.004, and thickness of 0.508 mm. In order to reduce the antenna cost, the material FR4 with the relative dielectric constant of 4.4, loss tangent of 0.02, and thickness of 0.8 mm is used for substrates 2 and 4. To establish the suspended structure, substrates 2 and 4 are hollowed by the same rectangular aperture to form two air cavities. In addition, the feed end is the transition structure of coplanar waveguide (CPW)-stripline-suspended line, and cuboid-shaped metallized vias are used in the whole text to replace general cylindrical metallized vias around air cavities. The feedline, radiator, and metal strip are all printed on substrate 3. In detail, as shown in Fig. 1(b) and (c), a metal strip with width of W_{s1} is placed on G5 layer, and its two ends are connected with two rectangular patches printed on G6 layer through metallized vias, respectively. Two rectangular patches are symmetrically placed at both sides of the quasi-I-shaped feedline; thus, both patches are gap-coupled by the feedline. In addition, a longitudinal slot with a length of L_{s8} is etched along the center of each patch. The entire structure of Proposed Antenna I is compact and fully symmetrical.

B. Dual-Band Filtering Response

To get a deep insight into the operating mechanism, the formation of the dual-band filtering response is analyzed.

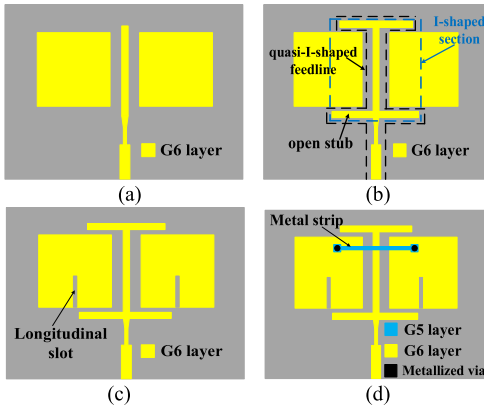


Fig. 2. Antenna evolution. (a) Ant 1. (b) Ant 2. (c) Ant 3. (d) Proposed Antenna I.

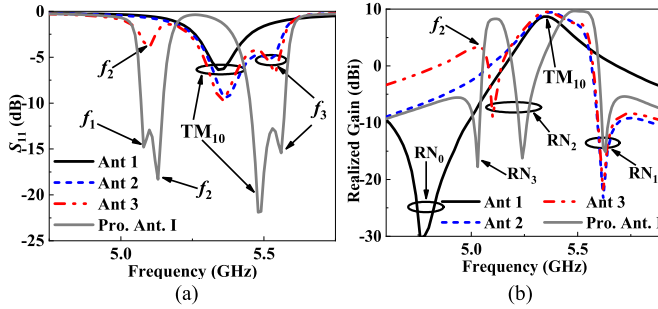


Fig. 3. Simulated results of reference antennas and Proposed Antenna I. (a) S_{11} . (b) Realized gain.

The configurations of three reference antennas and Proposed Antenna I are presented in Fig. 2, and their corresponding simulated results are given in Fig. 3. To obtain better impedance matching for easy comparison, some parameters of reference antennas are slightly fine-tuned.

Ant 1 is the original structure, in which two patches are gap-coupled through both sides of the conventional feedline. From Fig. 3, RN_0 is introduced in the lower stopband, and it can be concluded that the unique resonant mode is yielded by TM_{10} mode of the patch. According to the suspended structure of the SISL and the cavity mode theory of patch antennas, the frequency of TM_{10} mode can be evaluated by the following equations [2], [13]:

$$f_{mn} = \frac{c}{2\sqrt{\epsilon_{eff}}} \sqrt{\left(\frac{m}{a}\right)^2 + \left(\frac{n}{b}\right)^2} \quad (1)$$

$$\epsilon_{eff} = \frac{h_1 + h_2}{2h_1 + h_2} \left(1 + \frac{h_1 \epsilon_{r2}}{h_1 \epsilon_{r2} + h_2}\right) \quad (2)$$

where c denotes the light speed in the vacuum, m and n are the mode indices, a and b are the lengths of the nonradiation and radiation sides of the patch, respectively, h_1 is the thickness of the top substrate, and h_2 and ϵ_{r2} are the thickness and relative permittivity of the middle substrate, separately.

By loading two pair of open stubs on the conventional feedline, Ant 2 is established, and the quasi-I-shaped feedline is formed. As shown in Fig. 3, RN_1 is introduced in the upper stopband, and the upper passband is created by TM_{10} mode and the resonant mode f_3 . The electric field (E -field) distribution at f_3 is depicted in Fig. 4(a), demonstrating

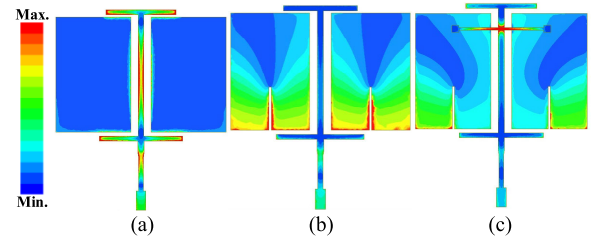


Fig. 4. E -field distributions on (a) Ant 2 at f_3 , (b) Ant 3 at f_2 , and (c) Proposed Antenna I at f_1 .

that f_3 is a resonant mode of the quasi-I-shaped feedline. However, it should be noted that when RN_1 appears in the upper stopband, RN_0 disappears. Because RN_0 and RN_1 are introduced when the I-shaped section operates at fundamental and second-order modes, respectively, and RN_0 is significantly shifted to a low frequency far from the operating band. The specific mechanism will be detailed in Section II-C.

Based on Ant 2, Ant 3 is built by etching a longitudinal slot perpendicular to the radiation edge along the center of the patch, which is illustrated in Fig. 2(c). As shown in Fig. 3, RN_2 is generated in the inner stopband between f_2 and TM_{10} . Moreover, as proved by the E -field distribution presented in Fig. 4(b), the resonant mode of the longitudinal slot marked as f_2 is produced, and its operating frequency can be evaluated by the following equation:

$$f_2 = \frac{c}{4L_{s8}\sqrt{\epsilon_{eff}}} \quad (3)$$

where L_{s8} is the length of the longitudinal slot.

Proposed Antenna I is obtained by printing a metal strip on G5 layer and connecting two ends of the metal strip with two patches through metallic vias, respectively, which is depicted in Fig. 2(d). The resonant mode f_1 is introduced by the metal strip, which can be verified by the E -field distribution displayed in Fig. 4(c). This metal strip operates at a half-wavelength under the excitation of a pair of common-mode (CM) signals, which will be further detailed in Section II-C. As a result, the lower passband is formed by f_1 and f_2 , and RN_3 is created in the lower stopband. Thus, total of three RNs are generated, and the desired dual-band filtering response with high selectivity and deep stopband rejection is obtained.

In the point of view of filter design, the two-order filtering response for both operating passbands is formed. All resonant modes of Proposed Antenna I can be considered as resonators. Although the longitudinal slot produces f_2 , it is etched on the patch and actually affects the surface current distribution of the patch, resulting in the far-field radiation of the patch at f_2 . Therefore, both f_2 and TM_{10} modes are attributed to the patch. To better illustrate the formation of the dual-band filtering response, the corresponding resonator-based topology of Proposed Antenna I is established, as shown in Fig. 5, where S and L denote the source and load, respectively, the black nodes represent the resonators, and the solid lines with different colors denote the main coupling in two operational passbands.

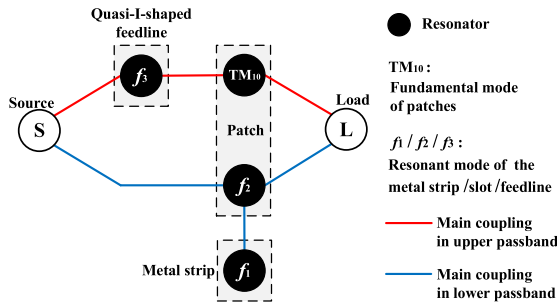
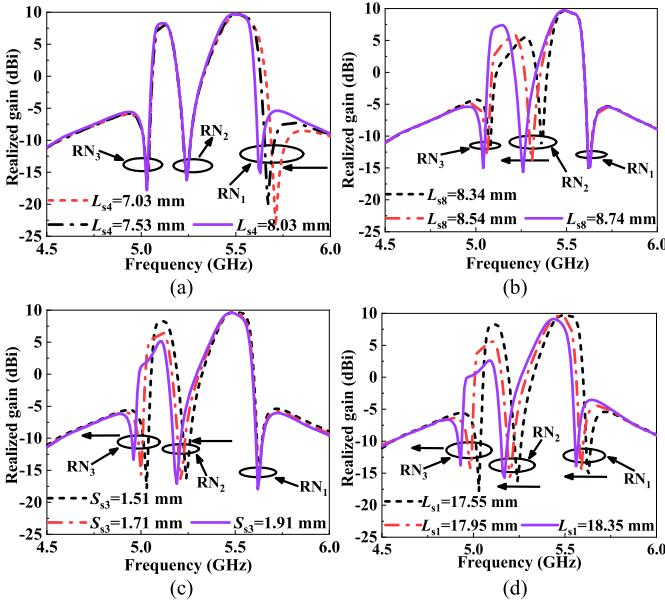


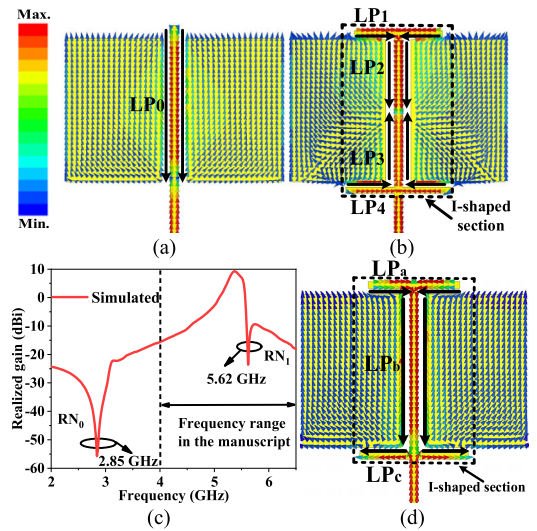
Fig. 5. Resonator-based topology of Proposed Antenna I.


 Fig. 6. Effects of parameters (a) L_{s4} , (b) L_{s8} , (c) S_{s3} , and (d) L_{s1} on RNs.

C. Radiation Nulls

As shown in Fig. 3(b), three RNs located at both sides of the two operational passbands can be introduced by Proposed Antenna I, which greatly improves the sideband roll-offs and out-of-band suppression. Fig. 6 displays the effects of some key parameters on the three RNs. It can be observed that RN_1 is independently adjusted by L_{s4} , while RN_2 can be controlled by L_{s8} with little impact on other two RNs. When the value of S_{s3} increases, both RN_2 and RN_3 simultaneously shift to lower frequencies, with little influence on RN_1 . Moreover, all three RNs can be simultaneously moved to higher frequencies by decreasing the value of L_{s1} . It demonstrates the adjustability of three RNs. To further reveal the antenna operating principle, the formation mechanism of three RNs is analyzed as follows.

RN_1 : RN_1 is generated after RN_0 has been shifted away, and the reason is as follows. RN_0 is generated by Ant 1 at 4.8 GHz, and the surface current distribution at RN_0 on Ant 1 is shown in Fig. 7(a), where the red strong current is mainly concentrated on the feedline with a half-cycle current path LP_0 , while the current on the patch is very weak. It illustrates that the signal is reflected back to the source, resulting in a very low level of the radiation from patches [29]. Thus, RN_0 is created. According to Fig. 3, RN_1 is initially produced by Ant 2 at 5.62 GHz. The corresponding surface current distribution is displayed in Fig. 7(b), revealing that RN_1 has


 Fig. 7. Current distributions at (a) RN_0 of 4.8 GHz on Ant 1 and (b) RN_1 on Ant 2. (c) Realized gain of Ant 2 at the frequencies of 2–6.5 GHz. (d) Current distribution of Ant 2 at RN_0 of 2.85 GHz.

the same generation mechanism with RN_0 of Ant 1. Compared with the feedline of Ant 1, the electrical length of the quasi-I-shaped feedline is increased significantly by loading two pairs of open stubs. Thus, the half-cycle current path related to RN_0 is greatly increased, and RN_0 is moved to 2.85 GHz, as displayed in Fig. 7(c). By comparing half-cycle current paths on the I-shaped section at RN_1 of 5.62 GHz and RN_0 of 2.85 GHz, as shown in Fig. 7(b) and (d), it can be found $(LP_a + LP_b + LP_c) \approx (LP_1 + LP_2) + (LP_3 + LP_4)$, where $(LP_1 + LP_2) \approx (LP_3 + LP_4)$, proving RN_1 and RN_0 of Ant 2 are introduced when the I-shaped section of quasi-I-shaped feedline operates at the second-order and fundamental modes, separately. Since RN_0 is far from the passband, RN_0 is not used in our work and is not given in the frequency range of the article. So, RN_1 is generated after RN_0 has been shifted away.

RN_2 : RN_2 is initially introduced by Ant 3. The surface current at RN_2 on Ant 3 is given in Fig. 8(a). The strong current in red mainly focuses around longitudinal slots, where the currents on both sides of each slot flow reversely, as shown by the black arrows, while on the upper side of the slots, the current on one patch is inverted with that of another patch, as shown by the purple arrows. Thus, the far-field radiation can be canceled each other out in the broadside direction to produce RN_2 . Note that RN_2 cannot be introduced by the asymmetrical structure with a single slotted patch presented in Fig. 8(b). The comparison of realized gain between symmetrical (Ant 3) and asymmetrical structures is given in Fig. 8(c), where the realized gain of the asymmetric structure is greater than zero at the frequency of RN_2 . Because the current on the upper side of the slot, as shown by the purple arrow in Fig. 8(d), cannot be further canceled and will contribute to the far-field radiation in the broadside direction. The comparison of 3-D radiation patterns of the asymmetric and symmetric structures at the corresponding frequency of RN_2 is shown in Fig. 9, further proving that RN_2 is generated by the far-field cancellation in the broadside direction caused by longitudinal slots and two patches together. Therefore, the formation of

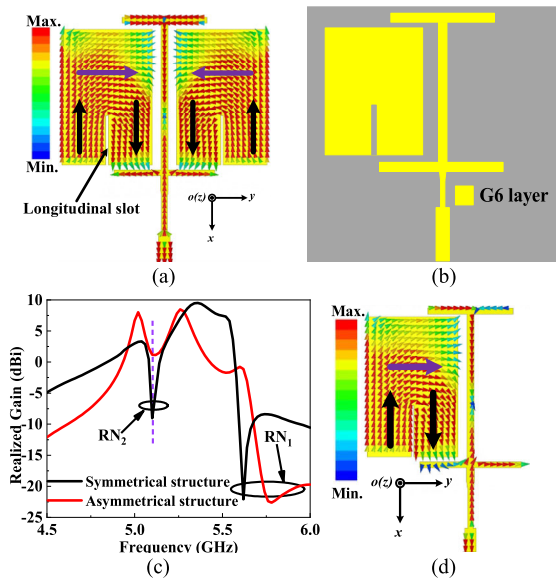


Fig. 8. (a) Surface current distribution at RN_2 on Ant 3 (symmetrical structure). (b) Asymmetrical structure. (c) Comparison of realized gain between symmetrical and asymmetrical structures. (d) Surface current distribution at the frequency of RN_2 on asymmetrical structure.

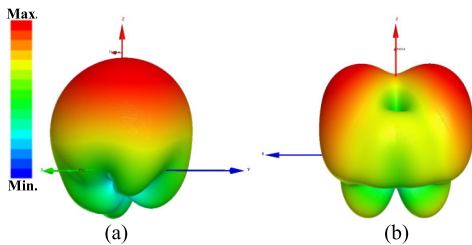


Fig. 9. Three-dimensional radiation patterns at the corresponding frequency of RN_2 . (a) Asymmetrical structure. (b) Symmetrical structure (Ant 3).

RN_2 requires the cooperation of the longitudinal slots and two patches.

RN_3 : According to Section II-B, RN_3 adjacent to f_1 is formed after loading the metal strip printed on G5 layer. Since both ends of the metal strip are connected to the same location on both patches through metallized vias, the metal strip is simultaneously excited by two signals with the same amplitude and the same phase provided by two patches, i.e., a pair of CM signals. The vector E -field distribution at f_1 on the metal strip is illustrated in Fig. 10(a), and the standard half-cycle vector E -field can be observed due to the superposition of standing waves. Thus, the metal strip acts as a half-wavelength resonator under the CM excitation, and its equivalent circuit can be established, as shown in Fig. 10(a). Due to the resonance of the metal strip, the red strong current is mainly concentrated on the metal strip at a certain frequency. Moreover, since the CM excitation occurs, the current on the metal strip flows to the opposite direction, which is depicted in Fig. 10(b), resulting in the current cancellation of generating RN_3 .

D. Simulated and Measured Results

For demonstration, a prototype of Proposed Antenna I is simulated, fabricated, and measured. The simulated and measured curves of S_{11} and realized gain are given in Fig. 11, and

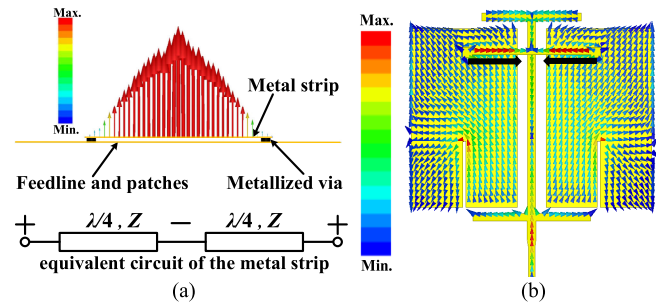


Fig. 10. (a) Vector E -field distribution at f_1 and equivalent circuit of the metal strip. (b) Surface current distribution at RN_3 on Proposed Antenna I.

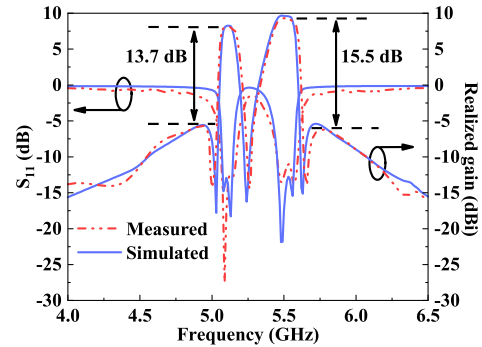


Fig. 11. Simulated and measured S_{11} and realized gain.

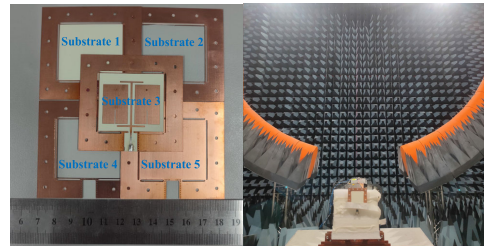


Fig. 12. Photographs of the fabricated antenna prototype and its experimental environment in the chamber.

the fabricated antenna is shown in Fig. 12. Two measured operational passbands with a fractional bandwidth of 1.95% and 2.71% are centered at 5.13 and 5.53 GHz, respectively. The maximum measured in-band gain reaches 8.06 and 9.32 dBi for the lower and upper passbands, separately, realizing the characteristic of high gain. In the stopbands, three RNs located at both sides of the two operating bands can be obtained at 5.01, 5.26, and 5.66 GHz, respectively, which achieves the fast roll-off rates at the sidebands. Furthermore, the good out-of-band suppression level more than 13.7 dB can be achieved within the stopband. As a result, the excellent dual-band filtering response is obtained by Proposed Antenna I, which is a good candidate for 5G dual-band applications.

The simulated and measured radiation patterns at 5.13 and 5.53 GHz are illustrated in Fig. 13. It can be seen that all radiation patterns are uniform and stable, and the good broadside radiation characteristics are achieved. The co-polarized fields of E-plane are at least 32 dB stronger than their cross-polarized ones, and the co-polarized levels in the broadside direction of H-plane are at least 13 dB stronger than their corresponding cross-polarized levels. Moreover, the front-to-back ratio at the measured frequencies is greater than 20 dB.

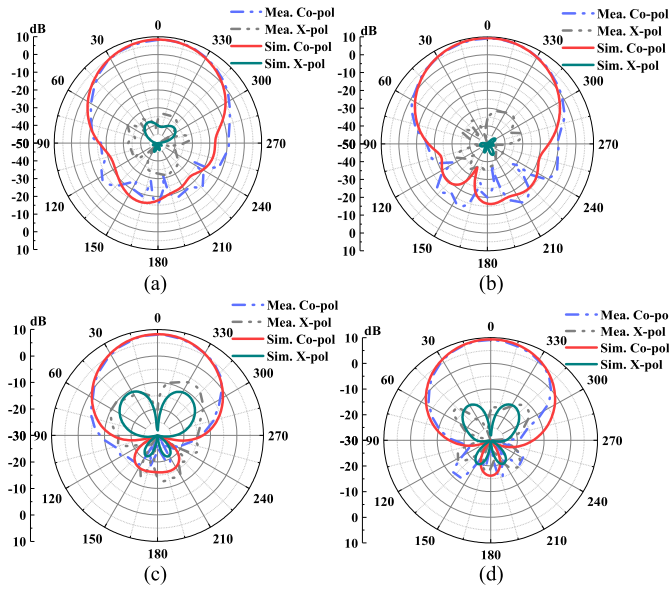


Fig. 13. Simulated and measured radiation patterns. (a) E-plane at 5.13 GHz. (b) E-plane at 5.53 GHz. (c) H-plane at 5.13 GHz. (d) H-plane at 5.53 GHz.

The good agreement can be observed between the simulated and measured ones.

III. DUAL-BAND SISL FILTERING ANTENNA WITH BROADSIDE AND BIDIRECTIONAL BEAMS

A. Antenna Configuration

The proposed dual-band SISL filtering antenna with broadside and bidirectional beams is presented in Fig. 14 and is named Proposed Antenna II. All substrates are the same material, thickness and form as the corresponding substrates in Proposed Antenna I. In Fig. 14(b), on M5 layer, T-shaped stubs with a length of L_{g4} are loaded on the patches, and a parasitic strip with a length of L_{g1} is placed near the lower side of each patch. In Fig. 14(c), a T-shaped metal strip connected with both patches through metallized vias and a quasi-T-shaped feedline is printed on M6 layer. Note that two disks etched with folded C-shaped slots and short matching branches are loaded on the quasi-T-shaped feedline. Both folded C-shaped slots are placed under the corresponding patch, where the narrow side of each patch is symmetrical about the slot up and down. The entire structure is also compact and fully symmetrical.

B. Dual-Band Filtering Response

In this part, Proposed Antenna II and reference antennas ANT_1–3 are analyzed to reveal the mechanism of the dual-band filtering response. Their structures are shown in Fig. 15, and the comparisons of simulated return loss and realized gain are given in Fig. 16. For Proposed Antenna II, as the lower passband shows the broadside beam, while the upper passband features the bidirectional beam with the maximum radiation at $\Phi = 90^\circ$ and $\theta = 30^\circ$, the simulated gain curves present the values at $\Phi = 90^\circ$ and $\theta = 30^\circ$ for comparing conveniently.

ANT_1 is the initial configuration, where two patches printed on M5 layer are gap-coupled by the quasi-T-shaped

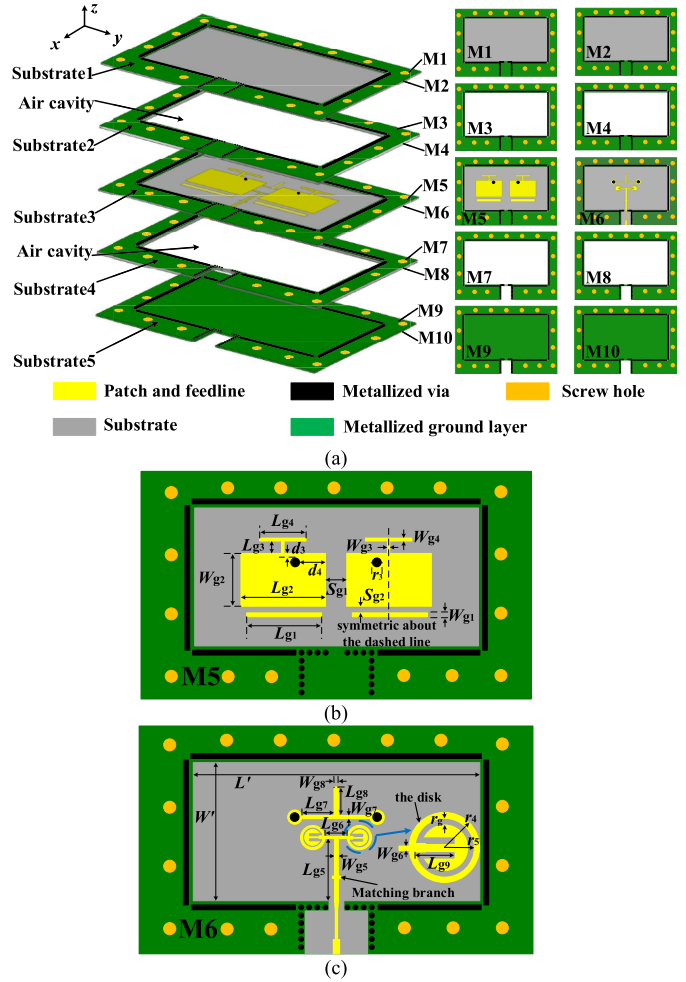


Fig. 14. Configuration of dual-band SISL filtering antenna with broadside and bidirectional beams (Proposed Antenna II). (a) Three-dimensional view and the configuration of each layer. (b) M5 layer. (c) M6 layer ($W' = 67$, $L' = 35$, $L_{g1} = 19.44$, $L_{g2} = 21.03$, $L_{g3} = 3$, $L_{g4} = 12.3$, $L_{g5} = 17.15$, $L_{g6} = 8.03$, $L_{g7} = 8.78$, $L_{g8} = 5.84$, $L_{g9} = 1.97$, $W_{g1} = 1.95$, $W_{g2} = 13.69$, $W_{g3} = 1.09$, $W_{g4} = 1.01$, $W_{g5} = 1.33$, $W_{g6} = 0.7$, $W_{g7} = 0.58$, $W_{g8} = 0.91$, $S_{g1} = 6.1$, $S_{g2} = 1.8$, $d_3 = 0.96$, $d_4 = 6.32$, $r_3 = 1$, $r_4 = 1.35$, $r_5 = 1.15$, and $r_g = 0.3$. Unit: mm).

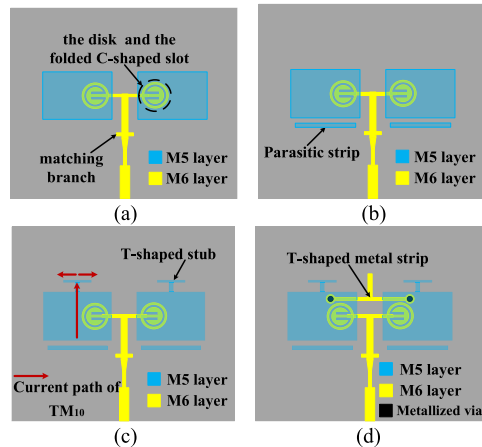


Fig. 15. Structure of (a) ANT_1, (b) ANT_2, (c) ANT_3, and (d) Proposed Antenna II.

feedline with folded C-shaped slots printed on M6 layer. From its simulated results, resonant mode f_c produced by the folded C-shaped slot and TM_{01} mode of the patch are yielded,

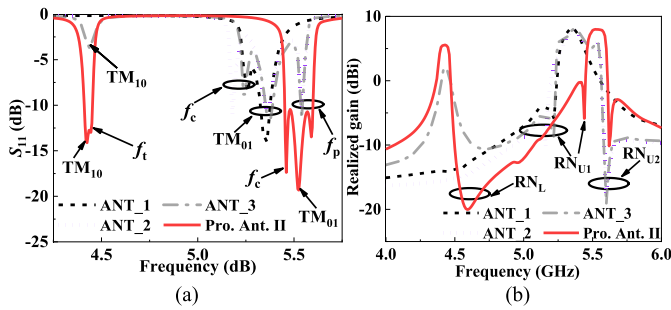


Fig. 16. Simulated results of the reference antennas and Proposed Antenna II. (a) S_{11} . (b) Realized gain ($\Phi = 90^\circ$ and $\theta = 30^\circ$).

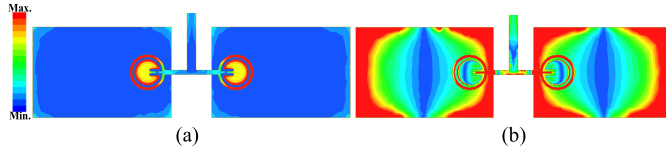


Fig. 17. E -field distribution on ANT_1 at (a) f_c and (b) TM_{01} mode.

which can be proved by their E -field distributions presented in Fig. 17. In addition, an RN named RN_{U1} is produced in the stopband. However, the selectivity of the upper stopband is poor.

To further improve the roll-off rates in the upper stopband and broaden the bandwidth, a parasitic strip is placed near the lower side of each patch to establish ANT_2. As depicted in Fig. 16, resonant mode f_p is introduced by the parasitic strip, and an RN named RN_{U2} is generated in the upper stopband. Thus, the frequency selectivity of the upper stopband is enhanced as expected, and the upper passband with good filtering response is attained.

Subsequently, by loading T-shaped stubs on both patches, the current path of TM_{10} mode can be effectively increased [30], while the size still remains small, as shown in Fig. 15(c). As a result, TM_{10} mode is successfully excited at a lower frequency of 4.4 GHz by ANT_3, which can be flexibly adjusted through the T-shaped stubs [30]. To further introduce an RN and broaden the bandwidth, a T-shaped metal strip connected with both patches through metallized vias is utilized to build Proposed Antenna II. As illustrated in Fig. 16, f_t is introduced by the T-shaped metal strip, and the lower passband is formed by f_t and TM_{10} mode. Moreover, RN_L is created at the right side of the lower passband. Finally, the desired dual-band filtering response with three RNs is obtained. According to the same theory as Proposed Antenna I, the two- and three-order filtering responses are achieved in lower and upper passbands, respectively, and the resonator-based topology of Proposed Antenna II can be given as Fig. 18.

C. Broadside and Bidirectional Beams

For the lower passband, the surface current distribution at the simulated center frequency of 4.42 GHz is illustrated in Fig. 19. It can be found that the surface current on the left patch rotates clockwise with the change of phase, while the

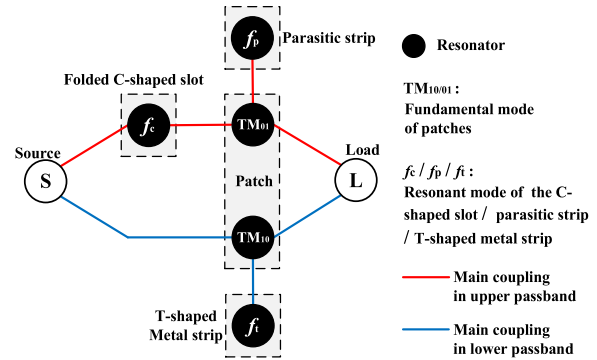


Fig. 18. Resonator-based topology of Proposed Antenna II.

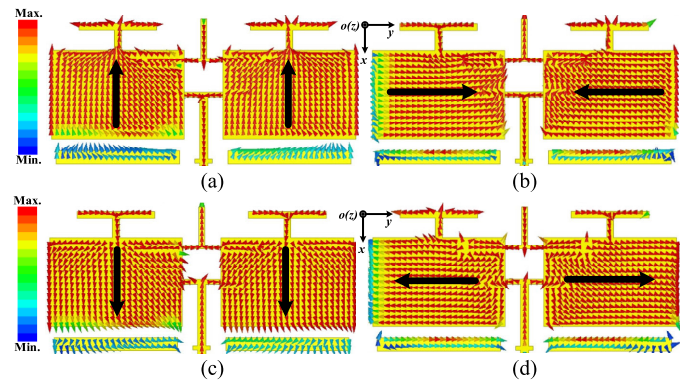


Fig. 19. Surface current distribution at 4.42 GHz. (a) Phase = 0° . (b) Phase = 90° . (c) Phase = 180° . (d) Phase = 270° .

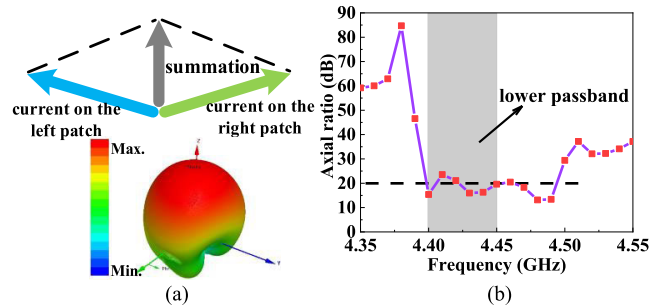


Fig. 20. (a) Current vector sum schematic (phase $\neq 90^\circ$ and 270°) and the 3-D radiation pattern at 4.42 GHz. (b) Simulated axial ratio values of the lower passband.

surface current on the right patch rotates counterclockwise as the phase varies. It is worth noting that the surface currents on the both patches are not inverted, except for the phases of 90° and 270° . Thus, although different current directions are achieved, the vector summation of currents in other phases (phases $\neq 90^\circ$ and 270°), which is presented in Fig. 20(a), is not zero and will contribute to the total far-field radiation in the broadside direction. It can be proved by the 3-D radiation pattern at 4.42 GHz shown in Fig. 20(a), which reveals that the lower passband owns the typical broadside radiation. Furthermore, according to the axial ratio of the lower passband, which is presented in Fig. 20(b), the total radiation field exhibited the good linear polarization with axial ratio values of about 20 dB is obtained in the lower passband.

For the upper passband, the surface current distribution at the simulated center frequency of 5.52 GHz is shown

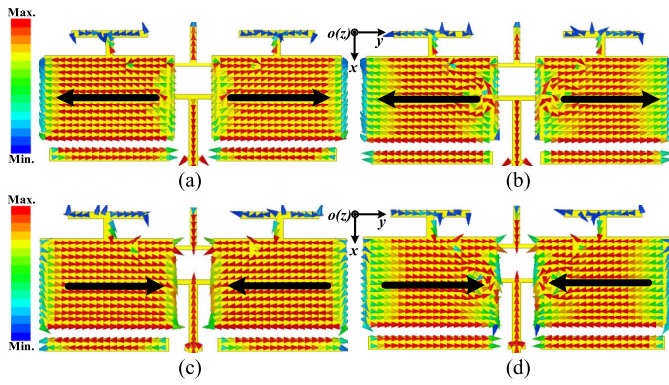


Fig. 21. Surface current distribution at 5.52 GHz. (a) Phase = 0°. (b) Phase = 90°. (c) Phase = 180°. (d) Phase = 270°.

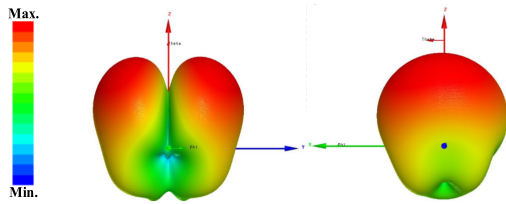


Fig. 22. Three-dimensional radiation pattern at 5.52 GHz.

in Fig. 21. It can be observed that the currents on both patches exhibit an equal magnitude but out of phase, and they always flow in the $\pm y$ -direction without changing with the phase. This phenomenon indicates that the far-field radiation of the two patches will be canceled out by each other in the broadside direction of the $+z$ -axis, resulting in the formation of the bidirectional beam. The 3-D pattern at 5.52 GHz is given in Fig. 22, where the angle between the beams in the direction of maximum radiation is 60°, realizing the good bidirectional radiation characteristics. Ultimately, broadside and bidirectional beams are achieved in the two operational passbands, respectively.

D. Radiation Nulls

From Fig. 16(b), it can be clearly observed that the deep RN_L is yielded at the right side of the lower passband. The surface current distribution at RN_L is displayed in Fig. 23(a). The red strong currents mainly focus on the T-shaped metal strip, while the extremely weak currents are on both patches, thus generating RN_L due to the very low radiation level of patches [29]. Note that the T-shaped metal strip is also excited by a pair of CM signals provided by two patches, and its mechanism is the same as detailed in Section II-C. Because of the CM excitation, the odd modes of the T-shaped metal strip are suppressed, and the even mode is excited. The even-mode equivalent circuit is presented in Fig. 23(b). In this work, the first even mode is used, its current path is shown by the black arrows in Fig. 23(a), and its frequency can be calculated by the following equation:

$$f_{even_1} = f_t = \frac{c}{(L_1 + 2L_2)\sqrt{\epsilon_{eff}}}. \quad (4)$$

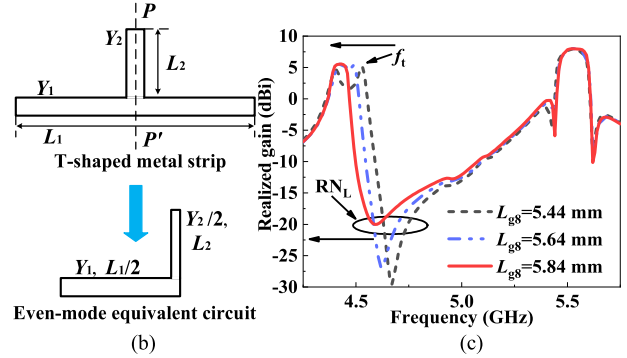
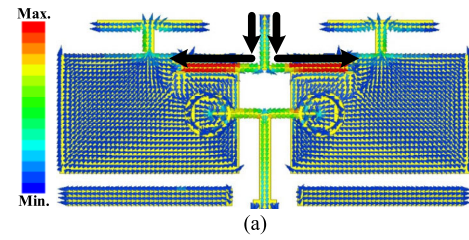


Fig. 23. (a) Surface current distribution at RN_L . (b) T-shaped metal strip and its even mode equivalent circuit. (c) Effects of L_{g8} on RN_L ($\Phi = 90^\circ$ and $\theta = 30^\circ$).

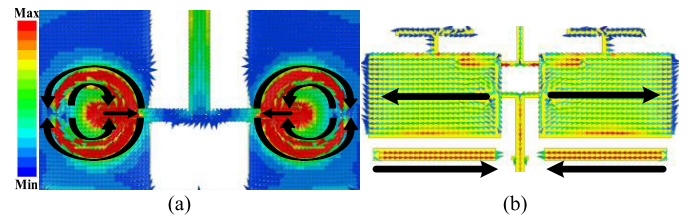


Fig. 24. Surface current distribution at (a) RN_{U1} and (b) RN_{U2} .

It reveals that f_t can be easily adjusted by changing L_2 (equivalent to L_{g8}) without altering the transverse size L_1 (equivalent to L_{g7}). Since the T-shaped metal strip contributes to the formation of RN_L , the location of RN_L can be adjusted by changing the frequency of the first even mode of the T-shaped metal strip. Therefore, by increasing L_{g8} , both RN_L and f_t exhibit a red shift, which is presented in Fig. 23(c).

Additionally, two RNs, i.e., RN_{U1} and RN_{U2} , are located on both sides of the upper passband. The surface current distribution at the two nulls is shown in Fig. 24. At RN_{U1} , the strong currents mostly flow inside and outside the folded C-shaped slots and have opposite flow directions. It means that the currents outside the slot can be eliminated by the currents inside the slot, thus producing RN_{U1} . At RN_{U2} , the current direction of each patch is opposite to that of each parasitic strip, and the parasitic strips have the same magnitude of energy as the patches [31]. Naturally, RN_{U2} is created by the far-field radiation cancellation of patches and parasitic strips. By changing the lengths of the folded C-shaped slot and the parasitic strip, i.e., L_{g9} and L_{g1} , RN_{U1} and RN_{U2} can be adjusted independently, as shown in Fig. 25.

E. Simulated and Measured Results

Proposed Antenna II is processed and tested to verify its performance. The simulated and measured results are illustrated

TABLE I
COMPARISONS BETWEEN THE PROPOSED FILTERING ANTENNAS AND RECENTLY REPORTED ANTENNAS

Ref	Type	Passband	FR*	No. of nulls	Radiation pattern	Size (packaged size?) ($\lambda_0 \times \lambda_0 \times \lambda_0$)	Max. gain (dBi)	Roll-off rate (dB/GHz)
[7]	SISL	2	NO	0	Broadside	0.55×0.55×0.04 (YES)	3.0/2.6	N.A.
[15]	SISL	1	YES	3	Broadside	1.87×1.57×0.04 (YES)	8.2	160/128
[16]	SISL	1	YES	2	Broadside	0.78×0.80×0.08 (YES)	10.4	87/188
[17]	SISL	1	YES	4	Broadside	1.3×1.0×0.05 (YES)	11.1	122/152
[18]	SISL	1	YES	3	Broadside	0.43×0.4×0.09 (YES)	4.2	115/90
[19]	SISL	2	YES	3	Broadside	0.71×0.58×0.06 (YES)	7.6/9.1	130/180/70~10
[20]	MS*	2	YES	3	Broadside	0.96×0.96×0.01 (NO)	2.2/4.8	80/195/40/268
[21]	MS*	2	YES	4	Broadside	0.3×0.4×0.01 (NO)	6.7/7.3	1028/243/572/163
[22]	SIW	2	YES	0	Broadside	1.29×1.29×0.01 (NO)	5.9/6.5	213/142/77/42
[23]	SIW	2	YES	3	Broadside	0.76×0.73×0.04 (NO)	4.8/4.9	108/284/425/581
[24]	MS*	2	NO	0	Broadside/Bidirectional	0.36×0.36×0.08 (NO)	4.3/5.7	N.A.
[25]	MS*	2	NO	0	Broadside/Bidirectional	0.37×0.28×0.08 (NO)	6.3/7.3	N.A.
Pro. Ant. I	SISL	2	YES	3	Broadside	0.6×0.68×0.05 (YES)	8.06/9.32	577/307/143/436
Pro. Ant. II	SISL	2	YES	3	Broadside/Bidirectional	0.52×0.99×0.05 (YES)	7.88/7.98	92/772/543/757 (Max. gain direction)

MS* denotes microstrip; FR* denotes filtering response; λ_0 represents the wavelength in free space at the center frequency of the lowest passband; The transvers sizes of SISL structures are calculated based on the length and width of air cavities; Roll-off rate is calculated as $(G_{\text{null}}-3)/|f_{\text{null}}-f_{3\text{dB}}|$. f_{null} denotes the frequency of radiation null or 10 dB gain attenuation (no radiation null). $f_{3\text{dB}}$ indicates the frequency of 3dB gain attenuation. G_{null} is the gain attenuation at f_{null} .

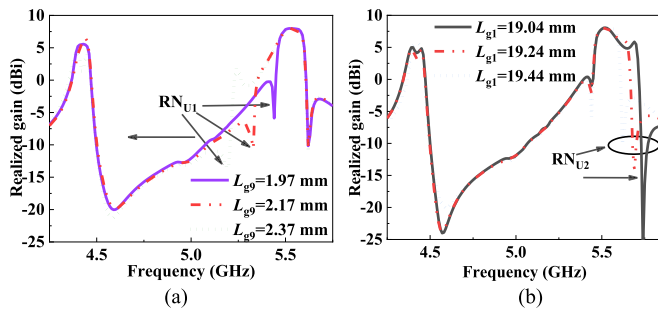


Fig. 25. (a) Effects of L_{g9} on RN_{U1} . (b) Effects of L_{g1} on RN_{U2} ($\Phi = 90^\circ$ and $\theta = 30^\circ$).

in Fig. 26, and the fabricated antenna is displayed in Fig. 27. Two measured operational passbands are centered at 4.43 and 5.53 GHz, respectively, and their -10 -dB impedance bandwidth is from 4.38 to 4.46 GHz and from 5.44 to 5.63 GHz, separately. In the direction of $\Phi = 0^\circ$ and $\theta = 0^\circ$, the realized gain of the broadside beam in the lower passband exhibits the maximum measured value of 7.88 dBi, while the bidirectional beam in the upper passband shows negative realized gain, as shown in Fig. 26(a). In Fig. 26(b), the bidirectional beam in the upper passband shows the maximum tested realized gain of 7.98 dBi in the direction of $\Phi = 90^\circ$ and $\theta = 30^\circ$, while the broadside beam in the lower passband has the realized gain about 5 dBi. Furthermore, three apparent RNs can be observed at 4.63, 5.41, and 5.65 GHz in the stopband, respectively, greatly improving the frequency selectivity and the stopband rejection levels.

The simulated and measured radiation patterns at 4.43 and 5.53 GHz are presented in Fig. 28. The radiation pattern at 4.43 GHz shows the typical broadside radiation, and its cross-polarization level is less than -15 dB in both E- and H-planes. At 5.53 GHz, the radiation pattern exhibits good bidirectional radiation characteristics. The maximum radiation field of the bidirectional beam can be observed at $\Phi = 90^\circ$

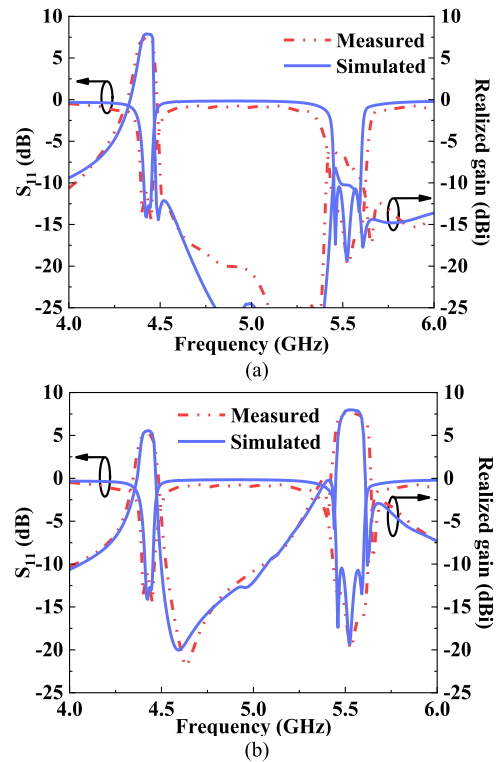


Fig. 26. Simulated and measured S_{11} and realized gain. (a) $\Phi = 0^\circ$ and $\theta = 0^\circ$. (b) $\Phi = 90^\circ$ and $\theta = 30^\circ$.

and $\theta = \pm 30^\circ$ in the E-plane, and its cross-polarization field is lower than -20 dB.

IV. COMPARISONS

The comparisons between our proposed antennas and some related antennas reported recently are listed in Table I. Although the SISL antenna presented in [7] has the dual-band response and a small size, it has no filtering performance. In [15], [16], [17], and [18], the SISL filtering antennas with

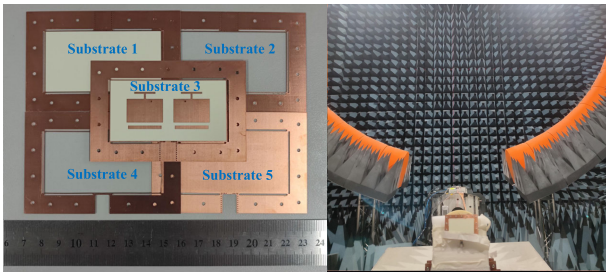


Fig. 27. Photographs of the assembled antenna prototype and the testing environment in the chamber.

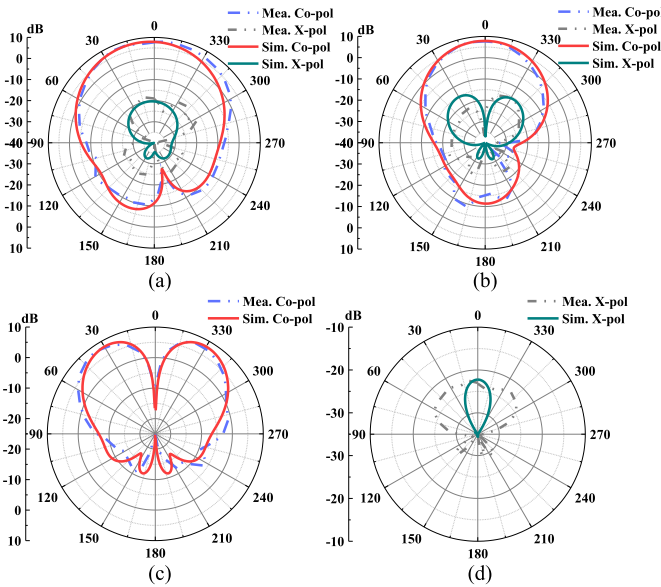


Fig. 28. Simulated and measured radiation patterns. (a) E-plane at 4.43 GHz. (b) H-plane at 4.43 GHz. (c) Co-polarization in E-plane at 5.53 GHz. (d) X-polarization in E-plane at 5.53 GHz.

multiple RNs were obtained, achieving the good filtering performance. However, these designs can only operate in a single operational passband. Despite one dual-band SISL filtering antenna was implemented in [19], its higher passband showed slow roll-off rates of about 70 and 10 dB/GHz, resulting in poor selectivity near the upper passband. In [20], [21], [22], and [23], the dual-band filtering response was realized by the microstrip and SIW structures. However, these structures suffer from the lower realized gain due to the higher dielectric loss of the microstrip and SIW and have no self-packaged property. In [24] and [25], the dual-band radiation-differentiated microstrip antennas is achieved, showing the good broadside and bidirectional radiation properties. However, the filtering response needs to be introduced. In our work, the proposed two SISL antennas exhibit the excellent dual-band filtering response with fast roll-off rates and three RNs, achieving high selectivity for each passband. Furthermore, both proposed antennas feature high gain of 8.06/9.32 and 7.88/7.98 dBi, respectively. In addition, with broadside and bidirectional beams, Proposed Antenna II realizes both filtering response and dual-band with different radiation, which can meet different wireless services in different application scenarios, such as 5G communications in crowded scenarios (bidirectional beam) and general scenarios (broadside beam).

V. CONCLUSION

Compact dual-band SISL filtering antennas with high selectivity based on dual gap-coupled patches are presented. By utilizing a quasi-I-shaped feedline, longitudinal slots etched on patches, and the metal strip connected with both patches, an excellent dual-band SISL filtering antenna with three RNs and broadside beams is realized, achieving sharp roll-offs and deep stopband rejection level. The measured -10 -dB impedance bandwidths are 5.08–5.18 GHz and 5.45–5.6 GHz, with the maximum gain of 8.06 and 9.32 dBi, respectively. Furthermore, by using folded C-shaped slots, parasitic strips, and the T-shaped metal strip connected with two patches, a dual-band filtering antenna with broadside and bidirectional beams is obtained on the SISL platform, generating three RNs in the stopband. Thus, both high selectivity and dual-band response with different radiations are achieved. The measured operating frequencies are 4.38–4.46 GHz and 5.44–5.63 GHz, achieving the maximum gain of 7.88 and 7.98 dBi, separately.

REFERENCES

- [1] K. Ma, N. Yan, and Y. Wang, “Recent progress in SISL circuits and systems: Review of passive and active circuits demonstrating SISL’s low loss and self-packaging and showcasing the merits of metallic, shielded, suspended lines,” *IEEE Microw. Mag.*, vol. 22, no. 4, pp. 49–71, Apr. 2021.
- [2] N. Yan, K. Ma, and H. Zhang, “A novel self-packaged substrate integrated suspended line quasi-yagi antenna,” *IEEE Trans. Compon., Packag., Manuf. Technol.*, vol. 6, no. 8, pp. 1261–1267, Aug. 2016.
- [3] N. Yan, K. Ma, and H. Fu, “A high-permittivity dielectric material-filled SISL antenna with cavity backing,” *IEEE Antennas Wireless Propag. Lett.*, vol. 20, no. 6, pp. 1033–1037, Jun. 2021.
- [4] X. Teng, Y. Luo, N. Yan, and K. Ma, “A cavity-backed antenna using SISL technology for 77 GHz band application,” *IEEE Trans. Antennas Propag.*, vol. 70, no. 5, pp. 3840–3845, May 2022.
- [5] Y. He, K. Ma, N. Yan, Y. Wang, and H. Zhang, “A cavity-backed endfire dipole antenna array using substrate-integrated suspended line technology for 24 GHz band applications,” *IEEE Trans. Antennas Propag.*, vol. 66, no. 9, pp. 4678–4686, Sep. 2018.
- [6] N. Yan, K. Ma, H. Zhang, and Z. Jian, “A novel substrate integrated suspended line wideband leaky-wave antenna,” *IEEE Antennas Wireless Propag. Lett.*, vol. 16, pp. 2642–2645, 2017.
- [7] Y. He, K. Ma, N. Yan, and H. Zhang, “Dual-band monopole antenna using substrate-integrated suspended line technology for WLAN application,” *IEEE Antennas Wireless Propag. Lett.*, vol. 16, pp. 2776–2779, 2017.
- [8] J. Hao, N. Yan, Y. Luo, H. Fu, and K. Ma, “A low-cost dual-band multimode high-gain stacked-patch antenna based on SISL for 5G applications,” *IEEE Antennas Wireless Propag. Lett.*, vol. 21, no. 1, pp. 4–8, Jan. 2022.
- [9] N. Yan, K. Ma, and Y. Luo, “An SISL sequentially rotated feeding circularly polarized stacked patch antenna array,” *IEEE Trans. Antennas Propag.*, vol. 68, no. 3, pp. 2060–2067, Mar. 2020.
- [10] Y. Chu, K. Ma, Y. Wang, and F. Meng, “A self-packaged low-loss and compact SISL DBBPF with multiple TZs,” *IEEE Microw. Wireless Compon. Lett.*, vol. 29, no. 3, pp. 192–194, Mar. 2019.
- [11] T. Feng, K. Ma, and Y. Wang, “A dual-band coupled line power divider using SISL technology,” *IEEE Trans. Circuits Syst. II, Exp. Briefs*, vol. 68, no. 2, pp. 657–661, Feb. 2021.
- [12] T. Feng, K. Ma, Y. Wang, and J. Hu, “Bandpass-filtering power amplifier with compact size and wideband harmonic suppression,” *IEEE Trans. Microw. Theory Techn.*, vol. 70, no. 2, pp. 1254–1268, Feb. 2022.
- [13] W. Yang et al., “A simple, compact filtering patch antenna based on mode analysis with wide out-of-band suppression,” *IEEE Trans. Antennas Propag.*, vol. 67, no. 10, pp. 6244–6253, Oct. 2019.
- [14] C. X. Mao, Y. Zhang, X. Y. Zhang, P. Xiao, Y. Wang, and S. Gao, “Filtering antennas: Design methods and recent developments,” *IEEE Microw. Mag.*, vol. 22, no. 11, pp. 52–63, Nov. 2021.

- [15] Y. Luo, T. Yin, N. Yan, W. An, and K. Ma, "A low-cost differentially fed dual-mode filtering MIMO antenna with enhanced isolation based on SISL platform," *IEEE Antennas Wireless Propag. Lett.*, vol. 21, no. 1, pp. 198–202, Jan. 2022.
- [16] M. Tian, N. Yan, Y. Luo, and K. Ma, "A low-cost high-gain filtering patch antenna using SISL technology for 5G application," *IEEE Antennas Wireless Propag. Lett.*, vol. 20, no. 12, pp. 2270–2274, Dec. 2021.
- [17] T. Wang, N. Yan, M. Tian, Y. Luo, and K. Ma, "A low-cost high-gain filtering patch antenna with enhanced frequency selectivity based on SISL for 5G application," *IEEE Antennas Wireless Propag. Lett.*, vol. 21, no. 9, pp. 1772–1776, Sep. 2022.
- [18] N. Yan, D. Song, Y. Luo, and K. Ma, "A low-cost miniaturized filtering dielectric resonator antenna based on SISL for 5G applications," *IEEE Trans. Antennas Propag.*, vol. 70, no. 12, pp. 11344–11352, Dec. 2022.
- [19] H. Zhou, N. Yan, and K. Ma, "An SISL dual-band filtering antenna with parasitic strips for 5G applications," *Int. J. RF Microw. Comput.-Aided Eng.*, vol. 32, no. 10, p. e23305, Oct. 2022.
- [20] K. Dhvaj, L. J. Jiang, and T. Itoh, "Dual-band filtering antenna with novel transmission zero characteristics," *IEEE Antennas Wireless Propag. Lett.*, vol. 17, no. 12, pp. 2469–2473, Dec. 2018.
- [21] X. Y. Zhang, Y. Zhang, Y.-M. Pan, and W. Duan, "Low-profile dual-band filtering patch antenna and its application to LTE MIMO system," *IEEE Trans. Antennas Propag.*, vol. 65, no. 1, pp. 103–113, Jan. 2017.
- [22] K. Dhvaj, H. Tian, and T. Itoh, "Low-profile dual-band filtering antenna using common planar cavity," *IEEE Antennas Wireless Propag. Lett.*, vol. 17, no. 6, pp. 1081–1084, Jun. 2018.
- [23] D. Zhao, F. Lin, H. Sun, and X. Y. Zhang, "A miniaturized dual-band SIW filtering antenna with improved out-of-band suppression," *IEEE Trans. Antennas Propag.*, vol. 70, no. 1, pp. 126–134, Jan. 2022.
- [24] Z. Zhang, M. Li, Q. Dai, M.-C. Tang, and L. Zhu, "Compact, wide-band, dual-band polarization and pattern diversity antenna for vehicle communications," *IEEE Trans. Antennas Propag.*, vol. 71, no. 5, pp. 4528–4533, May 2023.
- [25] S. Liu, S.-S. Qi, W. Wu, and D.-G. Fang, "Single-feed dual-band single/dual-beam U-slot antenna for wireless communication application," *IEEE Trans. Antennas Propag.*, vol. 63, no. 8, pp. 3759–3764, Aug. 2015.
- [26] X.-Q. Zhu, Y.-X. Guo, and W. Wu, "A novel dual-band antenna for wireless communication applications," *IEEE Antennas Wireless Propag. Lett.*, vol. 15, pp. 516–519, 2016.
- [27] J. Lin, Z. Qian, W. Cao, S. Shi, Q. Wang, and W. Zhong, "A low-profile dual-band dual-mode and dual-polarized antenna based on AMC," *IEEE Antennas Wireless Propag. Lett.*, vol. 16, pp. 2473–2476, 2017.
- [28] X. Yang, Y. Ji, L. Ge, X. Zeng, Y. Wu, and Y. Liu, "A dual-band radiation-differentiated patch antenna for future wireless scenes," *IEEE Antennas Wireless Propag. Lett.*, vol. 19, no. 6, pp. 1007–1011, Jun. 2020.
- [29] Z. Zheng, D. Li, X. Tan, M. Wang, and Y. Deng, "Compact low-profile differential filtering microstrip patch antenna with high selectivity and deep rejection using single-layer substrate," *IEEE Access*, vol. 9, pp. 76047–76055, 2021.
- [30] J.-F. Qian, F.-C. Chen, and Q.-X. Chu, "A novel tri-band patch antenna with broadside radiation and its application to filtering antenna," *IEEE Trans. Antennas Propag.*, vol. 66, no. 10, pp. 5580–5585, Oct. 2018.
- [31] D. Yang, H. Zhai, C. Guo, and H. Li, "A compact single-layer wideband microstrip antenna with filtering performance," *IEEE Antennas Wireless Propag. Lett.*, vol. 19, no. 5, pp. 801–805, May 2020.



Zhirui Zheng (Student Member, IEEE) received the B.S. degree in electric and information engineering from China West Normal University (CWNU), Nanchong, China, in 2019. He is currently pursuing the Ph.D. degree in information and communication engineering with Chongqing University (CQU), Chongqing, China.

His research interests include filtering antennas and filters.



Xiaoheng Tan received the B.E. and Ph.D. degrees in electrical engineering from Chongqing University, Chongqing, China, in 1998 and 2003, respectively.

He was a Visiting Scholar with the University of Queensland, Brisbane, QLD, Australia, from 2008 to 2009. He is currently a Professor with the School of Microelectronics and Communication Engineering, Chongqing University. His current research interests include antennas, filters, modern communications technologies and systems, communications signal processing, pattern recognition, and machine learning.



Daotong Li (Senior Member, IEEE) received the Ph.D. degree in electromagnetic field and microwave technology from the University of Electronic Science and Technology of China (UESTC), Chengdu, China, in 2016.

Since 2015, he has been a Visiting Researcher with the Department of Electrical and Computer Engineering, University of Illinois at Urbana-Champaign, Urbana, IL, USA, with financial support from the China Scholarship Council. He is currently with the Center of Communication and Tracking

Telemetry Command, Chongqing University, Chongqing, China. He has authored or coauthored over 60 peer-reviewed journals or conference papers. His current research interests include RF, microwave and millimeter-wave technology and applications, microwave power transmission (MPT), antennas, devices, circuits and systems, and passive and active (sub) millimeter-wave imaging and radiometer.

Dr. Li was a recipient of the UESTC Outstanding Graduate Awards by the Sichuan province and UESTC, in 2016, and the National Graduate Student Scholarship from the Ministry of Education, China, and "Tang Lixin" Scholarship. He is serving as a reviewer for several IEEE and IET journals and many international conferences as a TPC Member, a Session Organizer, and the Session Chair.



Mei Li (Member, IEEE) received the B.S. degree in electronic information science and technology from the Chengdu University of Information Technology, Chengdu, China, in 2010, and the Ph.D. degree in radio physics from the University of Electronic Science and Technology of China, Chengdu, in 2016.

From 2014 to 2016, she was a Visiting Graduate with the Applied Electromagnetics Research Group, University of California at San Diego, San Diego, CA, USA. From 2020 to 2022, she was a Ph.D. Research Fellow with the Department of Electrical

and Computer Engineering, University of Macau, Zhuhai, China. She is currently an Associate Professor with the School of Microelectronics and Communication Engineering, Chongqing University, Chongqing, China. Her research interests include metasurfaces-based electromagnetic devices, planar antennas, and arrays.



Qiang Chen (Senior Member, IEEE) received the B.E. degree from Xidian University, Xi'an, China, in 1986, and the M.E. and D.E. degrees from Tohoku University, Sendai, Japan, in 1991 and 1994, respectively.

He is currently the Chair Professor of the Electromagnetic Engineering Laboratory, Department of Communications Engineering, School of Engineering, Tohoku University. His research interests include antennas, microwave and millimeter wave, antenna measurement, and computational electromagnetics.

Dr. Chen is a fellow of the Institute of Electronics, Information and Communication Engineers (IEICE). He received the Best Paper Award and the Zenichi Kiyasu Award from the IEICE, in 2009. He served as the Chair of the IEICE Technical Committee on Photonics-Applied Electromagnetic Measurement from 2012 to 2014, the Chair of the IEICE Technical Committee on Wireless Power Transfer from 2016 to 2018, and the Chair of the Tokyo Chapter of the IEEE Antennas and Propagation Society from 2017 to 2018. He is the Chair of the IEICE Technical Committee on Antennas and Propagation.